Yield behaviour beneath hardness indentations in ductile metals, measured by three-dimensional computed X-ray tomography and digital volume correlation*

M. Mostafavi[1, 2], D.M. Collins[2], B. Cai[3], R. Bradley[3], R.C. Atwood[4], C. Reinhard[4], X. Jiang[2], M. Galano[2], P.D. Lee[3] and T.J. Marrow[2, #]

[1] Department of Mechanical Engineering, The University of Sheffield, UK
[2] Department of Materials, [#]Oxford Martin School, The University of Oxford, UK
[3] School of Materials, The University of Manchester, UK
[4] Diamond Light Source, Harwell Science and Innovation Campus, Oxfordshire, UK

Keywords: Computed Tomography, Indentation, Digital Image Correlation, Finite Element Analysis

Abstract

Plastic deformation in the vicinity of hardness indentations in two ductile metals, an aluminium-silicon carbide composite (Al-SiC) and a cast magnesium alloy (WE43), was characterised. Using in situ and ex situ X-ray computed tomography with digital volume correlation, the three-dimensional full-field displacements beneath the indentations were measured; these show strong agreement with simulated predictions using finite element models. It is demonstrated that plastic material properties, i.e. yield stress and hardening exponent, may be extracted via analysis of the deformation field.

1 Introduction

Hardness testing has long been used to interrogate materials to understand their deformation and fracture. The dimensions of an indentation, i.e. projected area and depth, sometimes augmented with analysis of the surface profiles from pile-up or sinking-in, are used to infer the net deformation that has occurred underneath the indenters [1-6]. With appropriate assumption or understanding of deformation processes such as strain-hardening, hardness tests on small samples are used to evaluate the effects of subtle changes in microstructure on the mechanical properties of engineering components; applications include, for instance, the effects of fast neutron irradiation and thermal ageing on structural steels [7, 8]. As a surface characterisation technique, the assumed deformation processes are not directly observed. Greater understanding of indentation testing, which would help support the accepted models (e.g. [9, 10]), would be obtained if the deformation paths within the material could be observed, in situ.

Digital image correlation (DIC) is a displacement measurement method with many applications [11]; it involves tracking of the movements of image subsets between successive images. In appropriate microstructures, X-ray computed tomography (XCT) can be combined with three-dimensional digital image correlation (digital volume correlation or DVC) [12] to measure the displacements within materials [13-17]; sufficient contrast may be achieved by X-ray attenuation or scattering from microstructural heterogeneities of the order of the voxel[1] size. As with DIC, the precision of displacement resolution increases with the multi-voxel interrogation subset size, enabling DVC to measure sub-voxel displacements [18]; for instance, we have recently shown this method can characterise the fracture behaviour of quasi-brittle materials [15, 19] and the 3D opening modes and displacements of indentation-initiated cracks in a brittle ceramic [20] and a short fatigue crack in a metallic sample [21].

In this paper, we have applied DVC to XCT observations to study the indentation behaviour in two ductile materials: an aluminium-silicon carbide composite (Materion's Al-SiC, 15% volume fraction reinforcement) and a magnesium alloy (Magnesium Elektron WE43). These materials were chosen because of the different heterogeneities of X-ray attenuation within their microstructures, which affects contrast in the XCT datasets. The measured three-dimensional displacement fields are compared with elastic-plastic finite element simulations for indentation in strain-hardening ductile materials. Our aim is to determine whether this methodology may be used to obtain material strain-hardening and yield properties, for instance by "reverse-modelling" methods; this would find applications in situations where small specimen tests are necessary, such as the monitoring of mechanical property degradation in extreme environments.

[1] A voxel is the three-dimensional equivalent to a pixel

2 Experiment

2.1 Materials

Magnesium is an important engineering material with applications including aviation gearbox casings [22], orthopedic biomaterials [23] and various lightweight components in the automotive industry such as engine blocks, transmission cases and wheel rims [24]. The Magnesium Elektron WE43 alloy is well suited to be characterized by XCT and DVC due to the low X-ray attenuation of Mg and the heterogeneous microstructure of the alloy that contains precipitates with strong X-ray attenuation (approximately 4wt% Yt and 3wt% rare earths such as Nd [25]). The Mg-alloy, which was aged for 8 hours at 350°C, is shown in Figure 1a.

A metal matrix composite was also used, comprising a Al6061 alloy matrix, reinforced by approximately 15 wt% SiC particles with a mean diameter of 500 nm. This Al-SiC composite has both high specific strength and modulus with potential aerospace applications [26]. The resulting microstructure following extrusion at 450°C is shown in Figure 1b. Cylindrical specimens of each material were machined with a 3 mm diameter and with heights of 3 mm for the Mg-alloy and 4 mm for the Al-SiC composite.

2.2 Tomography

Laboratory tomographs of the Mg-alloy were obtained using a Phoenix v|tome|x, (GE Measurement and Control) μCT machine operating at 90 kV and 80 μA, with a 512×512 pixel detector. At each 0.25° increment of rotation angle over 360°, two horizontally adjacent radiographs with 9 pixel overlap were recorded with an exposure time of 4 seconds, yielding 1440 projections, each of 1015×512 pixels. With a fan beam geometry, the specimen was placed close to the X-ray source to achieve a resolution of 3.95 μm per pixel. Back-projection reconstruction of the tomographs was performed using the Phoenix software (datos|x - GE Measurement and Control).

Synchrotron XCT of the Mg-alloy were obtained on the Diamond Manchester X-ray Imaging branch line (I13L) at the Diamond Light Source, operating with a monochromatic 20 keV parallel beam, with a 4008×2672 pixel detector (1.125 μm per pixel for the selected optics). Due to the relatively low flux obtained in this experiment, which took place during the commissioning phase, a 12 second exposure time per radiograph was necessary for sufficient signal. Each scan comprised 3600 radiographic projections at 0.05° increments over a 180° rotation. There is a very high absorption contrast difference between the Mg matrix and the beta-phase particles ($Mg_{14}Nd_2Y$) in the WE43 alloy [27]: Mg (density 1.74 g cm^{-3}) has an attenuation coefficient (including coherent scattering) of 2.76 cm^2 g^{-1} at 20 keV, compared to 24.6 cm^2 g^{-1} for the beta-phase (calculated density ~12.8 g cm^{-3}). The distance between the scintillator and the specimen was approximately 15 mm.

The Al-SiC composite sample was examined by synchrotron XCT at the Joint Engineering, Environmental and Processing (JEEP – I12) imaging beam line at the Diamond Light Source, operating with a monochromatic 53 keV parallel beam with a 4008×2672 pixel detector (0.9 μm pixel size for the selected optics). The expected absorption contrast difference between the Al alloy matrix and the SiC particles in the

composite is only 13% [27]: Al (density 2.7 g cm^{-3}) has an attenuation coefficient (including coherent scattering) of 0.334 cm^2 g^{-1} at 53 keV, compared to 0.331 cm^2 g^{-1} for SiC (density 3.1 g cm^{-3}). The distance between the scintillator and the specimen was therefore increased from 300 mm to approximately 1.5 m to enhance phase contrast [28, 29]. Each scan comprised 4500 projections at increments of 0.04 degrees over 180° with a 2-second exposure.

In the back projection reconstruction of the synchrotron tomographs [30], a combined Fourier-wavelet algorithm [31] was used to suppress ring artefacts (for more details see [31]). These arise from instrument features such as defective pixels in the scintillator; if not adequately supressed they can significantly increase noise in the DVC analysis as they do not displace with the material. As reconstruction artefacts formed at the centre of rotation may affect the DVC analysis, the site that was to be indented was positioned off-centre in each scan (0.3 mm for Mg and 0.2 mm for Al-SiC).

For the Mg-alloy, ex situ observations of the indentation were performed. A tomography scan of the sample was firstly obtained prior to indentation to provide a reference without deformation. The sample was removed from the instrument and subsequently indented using a standard Vickers indentation machine. This test was performed with a 20 kg force and a square-pyramidal diamond indenter. Finally, the specimen was returned to the instrument for tomography.

In situ observations of indentation were performed for the Al-SiC composite; the reference scan was recorded under a small pre-load (~10 N), which was applied to reduce rigid body movement between successive tomographs. A second scan was then obtained under load during Hertzian indentation via a 5 mm radius ZrO_2 ball. A 500 N indentation load, P, was applied, using a loading stage on the beam line that had been modified to accommodate the indenter. The load dropped to 480 N during the tomography scan (duration ~2.5 hours).

2.3 EBSD Characterisation

To independently assess the distribution of plastic deformation, electron backscatter diffraction (EBSD) characterisation was performed on the synchrotron XCT-scanned Mg alloy specimen. The sample was sectioned vertically, intersecting the indentation on the top surface across its deepest point; the section surface was ground and polished using progressively fine media, finishing with colloidal silica. The final surface finish was achieved using a Gatan precision ion polishing system (PIPS) at 5 keV and current density of 7 mA cm^{-2} for 2 hours, with the Ar-ion guns at 4° from the sample surface. EBSD was attempted on the Al-SiC specimen, but the pattern quality was insufficient for reliable indexing and this was therefore not pursued further.

The EBSD analysis was done using a JEOL-6500F scanning electron microscope in conjunction with TSL/EDAX OIM v6, with a beam current of 15 nA and an accelerating voltage of 20 keV and an acquisition time of ~0.9 seconds per point. A total area of ~420 μm × ~1000 μm with 3 μm step size was recorded, using two stitched maps to observe a region from the surface of the specimen, centred at the deepest point of the indentation. Grains were identified as continuous regions with a misorientation between adjacent points of less than 5°.

2.4 Digital Volume Correlation

Each synchrotron dataset had dimensions of 4016×4008×2672 voxels and each laboratory dataset was 1015×1015×512 voxels. To increase the efficiency of the DVC analysis, vertical (*z*) rigid body movements between datasets were first corrected by visual matching of image slices in a horizontal (*AA)* plane close to the indented surface. Each DVC analysis correlated the deformed dataset against its reference to map the relative 3D displacements; these were carried out using the Davis Strain Master 8.1 software [32], with the tomographs as 8 bit data.

DVC analyses the deformation field between successive datasets by using progressively smaller subsets (i.e. interrogation volumes), obtaining their relative positions and deformation. Reducing the final interrogation volume size increases the spatial resolution of the displacement field, though random errors (noise) also increase [10]. Overlapping interrogation subsets can improve the spatial resolution in smoothly changing fields, allowing the use of larger interrogation subsets to reduce measurement noise. Increasing the number of passes may also reduce noise, with a diminishing effect with increasing passes. Sequences of interrogation subsets, overlaps and passes were chosen that optimised the precision and spatial resolution of each displacement field dataset. Consequently, the laboratory Mg data were analysed with a 128×128×128 interrogation subset (50% overlap and 2 passes) followed by a 32×32×32 subset (75% overlap and 2 passes) and then a 16×16×16 subset (50% overlap and 2 passes). Displacement vectors with a correlation coefficient of less than 0.5 were deleted and replaced by an interpolation of neighbouring vectors. No cropping of the laboratory XCT dataset was done, but each synchrotron dataset was cropped prior to analysis to select the chosen region of interest; the synchrotron Mg data were cropped to 3000×3000×1000 voxels; the analysis used a 512×512×512 interrogation subset (50% overlap, single pass) followed by a 128×128×128 subset (50% overlap, 2 passes) and finally a 64×64×64 subset (50% overlap, 3 passes). Displacement vectors with a correlation coefficient of less than 0.5 were replaced as before. The Al-SiC data were cropped to 3504×3504×2000 voxels and analysed by a 256×256×256 interrogation subset (50% overlap, 2 passes) then a 64×64×64 interrogation subset (50% overlap and 2 passes). Due to the lower contrast, a slightly more stringent criterion was applied to reduce noise, replacing displacement vectors with a correlation coefficient of less than 0.6 by interpolation of the neighbourhood vectors. The final interrogation subsets for the three experiments were similar in size; ~63 μm, 72 μm and 58 μm for the laboratory and synchrotron Mg and the Al-SiC analyses respectively. The end results were three-dimensional matrices of displacement vectors; the matrix sizes were 127×127×64 for the Mg-laboratory, 94×94×31 for Mg-synchrotron and 109×109×62 for Al-SiC datasets. The displacement field was then corrected for fine rigid body movements and rotations, using the method described in the Appendix, so the displacement field coordinate system was aligned to the loading axis of the indentation.

3 Results

3.1 X-ray Computed Tomography

The coordinate system and reference planes for sectioning are shown in Figure 2a, with a visualization of the indentation in the Mg-alloy sample (laboratory data).

Examples of horizontal (AA) slices of three specimens are shown in Figure 2b-d, with higher magnification images inset to show the quality of the images. For the Mg-alloy, the higher resolution of the synchrotron tomographs relative to the laboratory tomographs is evident (Figure 2b vs. Figure 2c); image artefacts from the highly attenuating particles are also less prominent (these are commonly referred to as "streak artefacts" [33]). In the Al-SiC (Figure 2d), the SiC particles have not been fully resolved, due to their small size and low contrast.

Vertical (i.e. *BB*) sections can be used to measure the indentation depth, h_t; this is 115±8 μm for the Mg-laboratory experiment (Figure 3a), 108±5 μm for the Mg-synchrotron experiment, both after removal of the indentation (Figure 3b), and 47±4 μm for the Al-SiC sample (Figure 3c) with the in situ indentation; similar inspection of the reference image for the Al-SiC sample (under a small load of 10 N as described above) measures the initial indentation depth to be 7±5 μm.

Determining the quality of tomographic data for optimum DVC analysis is presently a matter of judgement. Histograms of the grey-scale intensities for the example tomography slices are inset within Figure 2; the standard deviation of the intensity for the Al-SiC is low due to its lack of contrasting features. Both the Mg synchrotron and Mg laboratory have higher, and similar standard deviations; this is expected as the tomographic reconstruction involves normalisation of intensity ranges, so it is also instructive to examine the quality of the X-ray radiographs. The frequency distribution of detector saturation (after background correction) for a profile along each sample's vertical diameter is presented in Figure 3d; there is very little signal (~1.7%, standard deviation 0.35%) for the synchrotron Mg radiograph compared to the Al-SiC (~15.4%, standard deviation 1.65%), which is ~30% thicker than both Mg samples. The laboratory Mg radiograph has the strongest signal (~ 38.0%, standard deviation 1.15%). Given the very much lower signal for the Mg synchrotron radiographs, higher levels of random noise in the tomographs may be expected.

3.2 EBSD Characterisation

The EBSD inverse pole figure map of the Mg-alloy sample from the synchrotron experiment is shown in Figure 4a. The grains have a unimodal size distribution with a mean diameter, calculated from the area of each grain, of 66 μm (standard deviation 22 μm). The observed grains do not present any strong texture.

To assess the plastic deformation within the Mg grains, a kernel average misorientation (KAM) plot was obtained (Figure 4b); this calculates the magnitude of crystal misorientation within each grain (i.e. the kernel), providing an indication of the lattice distortion within a grain. This can be correlated to regions with a high dislocation density [34], and so provides a means to identify regions with plastic strains. The data show, qualitatively, that those grains closer to the indentation have been plastically deformed. The regions coloured white in the KAM map correspond to points in the EBSD map that have not been reliably indexed due to poor diffraction pattern quality; blurring of diffraction patterns occurs when the dislocation density is high [35]. The variation of the KAM as a function of distance from the indentation is shown in Figure 4c in which the data were averaged within 48 μm × 48 μm non-overlapping regions; these are of a similar order to the interrogation subset site of the digital image correlation analysis performed on this sample, and also the grain size. The error bars are the standard deviation of up to 256 measurements at each point. A

general trend for decreasing KAM with distance from the indentation is obtained, though low values are measured in close proximity to the indentation (i.e. between 0 and 300 μm); by selecting an arbitrary 0.8° KAM threshold the extent of the plastic zone below the indent is estimated to be approximately 600 μm.

3.3 Digital Volume Correlation

The displacement measurements for the laboratory data of the Mg sample have an uncertainty of the order of 0.1 voxel (i.e. ~0.4 μm). This is comparable to precision reported in the literature for DVC on good quality images with similar interrogation subset size [10, 19]. The synchrotron data, which are of poorer quality for DVC analysis due to the low signal to noise ratio of the Mg radiographs and the low contrast of the Al-SiC composite, have an uncertainty of approximately 2 voxels; i.e. ~2 μm for both Mg and Al-SiC.

The in-plane horizontal displacements (U_x and U_y) were converted to polar coordinates and averaged radially (after conversion the displacements with spatial distance less than 1 μm were binned together) to obtain a radial displacement (U_r). The axis of the indentation was taken as the origin. The Hertzian indentation displacement field is symmetric, hence radial averaging was performed for $\omega = 0°$ to 360° where ω is the angular coordinate (Figure 2a). Although the Vickers indentation geometry is not fully axisymmetric, it can be considered as such for those points that are remote from the point of contact [36]; radial averaging was therefore applied to the Vickers indentation displacement fields as well. As a consequence of the radial averaging, the uncertainty in the reported displacements was reduced to below one voxel (i.e. ~1 μm) for both Mg and Al-SiC (for the detailed analysis of displacement measurement noise, see the Appendix).

The radially averaged displacement vectors are overlaid on maps of the compressive strain field (Figure 5), calculated by the finite difference method using adjacent points of the radially averaged data; this was done using an in-house MATLAB code, but this method is implemented also in the DVC software [32]. High tensile strains are observed below the indention, tending to a uniformly distributed compressive strain with increasing distance. These strain fields should be regarded as qualitative, since the finite difference method is quite affected by experimental displacement noise in the differentiation operation. For quantitative analysis, it is preferable to work with the directly measured displacement fields, as will be considered in the following section.

4 Finite Element Simulation

Three dimensional finite element simulations of the Vickers and Hertzian indentations were carried out using ABAQUS v 6.10 [37]. In both cases, finite sliding, frictionless contact was assumed between the indenter and the sample. Nonlinear geometry was considered, in order to account for the effect of high levels of deformation on the stiffness matrix. It is important to maintain consistency of the physical and modelling length scales. If only a small number of grains are affected by the indentation, the procedure cannot be modelled using a continuum finite element simulation. The fine grain size and lack of strong texture shown by the EBSD analysis of the specimens support the appropriateness of the finite element simulations carried out. In the

absence of such conditions a more sophisticated model (e.g. crystal plasticity) would be appropriate.

The Vickers indenter (diamond, elastic modulus E_i>1000 GPa) was modelled as a rigid body with 1800 elements (Figure 6a shows one half of the model). The Mg specimen was simulated using 18000 solid eight-node brick elements, with bilinear elastic-plastic properties: Young's modulus, E_s, 44 GPa, Poisson's ratio, v_s, 0.27 with yield stress 178 MPa and 7% plastic strain at the ultimate tensile stress of 250 MPa (as reported by the manufacturer [25] in the peak-aged condition). Both Kinematic and Isotropic hardening cases were considered since no information on the material behaviour after unloading was available. The indenter was driven into the specimen until the reaction force reached 200 N (i.e. within 2% of the 20 kg indentation load); the indenter was then displaced fully out of the specimen to simulate the unloading process. Displacement controlled boundary conditions were used to achieve convergence. The resulting indentation depth was 110 μm, which is close to the experimentally measured values for the laboratory and synchrotron experiments. The maximum extent of plasticity was 830 μm below the surface of the sample, measured from the original surface of the specimen; yielded elements in the FE simulation were identified using the J2 flow theory of plasticity [38], which compares the von Mises stress to the tensile yield stress.

The Hertzian indenter (ZrO_2, elastic modulus, E_i, 400 GPa and Poisson ratio, v_i, 0.28) was also modelled as rigid with 1200 elements (Figure 6b shows one half of the model). The Al-SiC deformation was simulated with the same mesh that was used for the Mg specimens, with the following nonlinear elastic (Ramberg-Osgood) material properties: elastic Young's modulus 102 GPa, yield stress (0.2% proof stress) 230 MPa and hardening exponent 9.7. These were obtained by curve-fitting to tensile data [39], and agree with published results for a similar material [40]. The Poisson's ratio used was 0.27, which is the literature value for aluminium alloys such as Al6061 [40]. The nonlinear elastic material model was employed since the observations were performed in situ with no unloading. The indenter was displaced 47 μm vertically, obtaining a reaction force of 484 N, which agrees well with the experimentally recorded load. The maximum extent of plasticity was 750 μm below the surface of the sample, measured from the original surface of the specimen.

To compare the displacement fields of the simulations and experiments, two paths were selected: an axial path along the vertical z-axis in the direction of the indentation and a radial path from this axis at a distance z_0 of approximately 250 μm below the indentation (z_0 =256 μm for the Mg samples and z_0 =232 μm for Al-SiC sample, due to the different pitches of the displacement data matrices). The polar (U_r) and compressive (U_z) displacements for radial paths and also the compressive displacements (U_z) along the axial path are compared with the FE simulations for the Mg experiments and the Al-SiC experiment in Figure 7 and Figure 8 respectively. In each case the reported displacements are relative to the average displacement of the sample at a position remote from the indentation (i.e. at z = 1 mm). The averaged radial displacement along the direction of the indentation is zero in FE simulations, since the indentation is perfectly aligned. The corresponding average radial displacements in the experiments, measured along the entire depth of the observed area, were 1.4 μm, 3.7 μm and 0.9 μm for the Mg laboratory, Mg synchrotron and Al-SiC experiments respectively; this demonstrates the effectiveness of the removal of

rigid body rotations (see Appendix) such that the reported displacement field is well aligned to the direction of the indentation in each case.

The FE simulations predict that the radial displacement increases to a maximum and then decreases with increasing radial distance, and also a progressive decrease in the vertical displacements with increasing vertical and radial distance from the indentation. The measured vertical and radial displacements agree well with the finite element simulations for both Mg and Al-SiC (Figure 7 and Figure 8), except beneath the indentation where the measured vertical displacements are significantly smaller than the simulation results within a distance of approximately 200 μm of the indentation. The discrepancy between the finite element results and those measured by combined XCT and DVC very close to the indentation is due to high levels of deformation in this area. Large deformations, if not observed incrementally, can result in loss of correlation between successive datasets. The differences between the Kinematic and Isotropic hardening models for the Mg-alloy are not significant, and it cannot be judged that either model better fits the experimental data. The differences in the measurements for the indentations in Mg, studied by laboratory and synchrotron X-rays, are most apparent in the radial displacements, which are smaller than the vertical displacements. This may be due to microstructural differences between the small sampled volumes in the two samples.

5 Discussion and Further Analysis

The agreement between the measured and predicted displacement fields demonstrates the effectiveness of DVC. Due to the low attenuation contrast between the Al and SiC and with limited phase contrast, the microstructure of the Al-SiC is barely resolved, yet the random arrangement of SiC produces sufficient heterogeneous intensity for correlation to measure the relative displacements of microstructure regions. Similarly, the noisy data obtained in the commissioning-phase synchrotron observations of the Mg alloy have been successfully analysed. Both EBSD and DVC were unsuccessful in resolving deformation in regions with very high levels of plasticity i.e. close to the indentation. Recent calculations for spherical indenters [41, 42] have shown that the highest stresses/strains under the indenter occur at approximately the depth of the contact radius before unload a:

$$a = \left(\frac{3PR^*}{4E^*} \right)^{1/3}$$

where P is the indentation force and R^* and E^* are effective radius and Young's modulus respectively:

$$\frac{1}{E^*} = \frac{1-\nu_s^2}{E_s} + \frac{1-\nu_i^2}{E_i}, \quad \frac{1}{R^*} = \frac{1}{R_s} + \frac{1}{R_i}$$

where s and i subscripts denote sample and indentor; E is Young's modulus, ν, is Poisson ratio and R is radius (for a flat sample, $R^*=R_i$). Assuming a fully elastic regime for the Hertzian indentation of the Al-SiC, the contact radius of approximately 0.25 mm corresponds with the depth of the volume in DVC that gives unreliable measurements. This is due to high levels of plastic deformation that changes the

contrast features of the material to a level that image correlation algorithms fail to follow them. This can be avoided if incremental loading is performed which will allow for the features to deform gradually and be detectable by the correlation algorithms.

This study shows that high resolution computed X-ray synchrotron tomography can reliably quantify the localised displacements associated with indentation testing in engineering materials. Plastic deformations in two ductile materials have been measured and agree with FE simulations with constant strain hardening rates; more sophisticated FE simulations might achieve a better agreement [3]. This raises the possibility that the material properties, particularly the stress-strain behaviour, might be obtained by FEA (Finite Element Analysis) "reverse-modelling" [9, 10] of the indentation displacement field. To investigate the suitability of a combined XCT-DVC-FEA method to characterise material properties of ductile materials from indentations, a sensitivity study was conducted. Further finite element simulations of the indentations, were performed with a range of plastic material properties. For the ex situ observations of the Mg-alloy, kinematic hardening was assumed and the experimental ex situ loading and unloading was simulated, as previously. The ultimate tensile stress was varied from the yield stress (178 MPa, i.e. elastic-perfectly plastic) up to 400 MPa to simulate a range of strain-hardening behaviour.

The compressive displacements calculated along the indentation were axis extracted from these analyses and normalised with respect to U_o:

$$U_o = \sqrt{\frac{P}{E}}$$

where P is the indenter's reaction force at which the experimentally measured indentation depth is achieved in each simulation and E is the elastic modulus.

The normalised compressive displacements ($\overline{U_z}$) are shown in Figure 9a, and are compared with the experimental data. Due to the reverse plasticity that occurs on unloading, the dependencies of the displacement fields on material properties are insufficiently strong for a reverse-modelling analysis to be successful.

For the in situ Al-SiC study, the nonlinear elastic (i.e. Ramberg-Osgood material) model was considered with a range of hardening exponents from n=2 up to 50 with a constant yield stress 230 MPa in one set of simulations; a second set of simulations considered a constant hardening exponent (n= 9.7) and varied the yield stress from σ_y = 100 to 400 MPa. The obtained radially averaged polar (U_r) and compressive displacements (U_z) along a horizontal path beneath the indenter (232 μm below the specimen surface) are normalised in the same way as the Mg data (denoted by $\overline{U_r}$ and $\overline{U_z}$ respectively). They are shown in Figure 9b and c, and are compared with the experimental data. Figure 9d shows the normalised compressive displacement ($\overline{U_z}$) along an axial path passing through the deepest point of the indentation. There is a clear dependence of the magnitude and form of the displacement profiles on yield stress and hardening exponent, particularly at lower strain hardening exponents,

indicating that a reverse-modelling analysis by fitting to the experimental data could be successful.

A further set of 72 finite element simulations was therefore performed for the Al-SiC indentation, with combinations from n=2 to 50 (9 values, as before) and σ_y =100 to 400 MPa (8 values, as before). The elastic modulus and Poisson's ratio were constant (E=102 GPa, ν=0.27); they are insensitive to materials processing and can also be obtained from independent testing (E can be measured in indentation experiments from the unloading compliance [43], for example). The normalised compressive displacements along the vertical axial path below the indenter from z=0.2 mm to z= 1 mm were compared with the experimental data, as these are the larger displacements in the dataset.

A matrix of residual errors was formed (i.e. residual error matrix), quantifying the difference between the experimentally measured and simulated normalised compressive displacements:

$$R_{i,j} = \sqrt{\sum_{k=1}^{N} \left(M_{i,j,k}^{FE} - M_{i,j,k}^{Exp} \right)^2}$$

where $M_{i,j,k}^{FE}$ is the three dimensional matrix that stores from the simulation the normalised vertical displacements along the axial path (k=1 to N= 53, at the same locations of the experimentally measured points between z=0.2 mm to 1 mm) as a function of hardening exponent (j=1 to 9) and yield stress (i=1 to 8). The experimentally measured normalised displacement field is stored similarly in the matrix $M_{i,j,k}^{Exp}$. A third order polynomial surface was fitted to the residual errors matrix, achieving a correlation coefficient of 0.99, which allowed interpolation between evaluated points (Figure 10). The single global minimum, at which the simulation best fits the experiment with uniform weighting for hardening exponent and yield stress, was obtained for n=13.5 and σ_y =210 MPa. This agrees with the known properties of the Al-SiC material; the extracted yield stress is 9% lower from the expected 230 MPa yield stress, though the hardening exponent is 40% higher than the expected value of 9.7. A more accurate optimisation process, with informed weightings to different parts of the displacement field that are more sensitive to hardening exponent or yield stress and also the use of 5D matrices to utilise the full-field displacements, should result in more accurate extraction of material parameters. Such an optimisation process is beyond the scope of the present experimental paper and dataset, but is being developed by the authors for future studies.

The preceding analysis has demonstrated that material properties may be extracted by a reverse-modelling analysis of the three-dimensional displacement fields of hardness indentations in suitable microstructures, measured in situ. Hardness testing is particularly suited to small specimen tests, hence the effects of temperature or thermal ageing or irradiation damage might then be studied in samples that have been extracted to monitor materials degradation in engineering components. This methodology may also be useful for the interpretation of indentation deformation in more complex structures with gradients of material properties, such as strain-hardened surfaces and graded microstructures. Studies of localised plasticity at crack tips or notches in ductile materials are also feasible.

6 Conclusion

A method has been demonstrated by which the plastic properties of a ductile metal can be extracted by reverse-modelling analysis of the displacement field below a hardness indentation, measured by DVC analysis of in situ XCT observations.

Acknowledgements

This work was carried out using the tomography facilities of the Diamond Light Source and the Research Centre at Harwell. The authors acknowledge the beam time awarded at the Joint Engineering, Environmental and Processing (I12 – JEEP) beam line (Experiment EE7119) and the I13L Diamond Manchester X-ray Imaging branch line (Commissioning experiment MT8431). Dr H. Cetinel, Mr S. Barhli and Mrs T Sui are thanked for their help in conducting the experiments. The inputs of Dr C. Rau, Dr M Drakopoulos, Dr K. Wanelik and Dr A. de-Fanis at the Diamond Light Source were appreciated, as were useful discussions with Professor A. Korsunsky and Mr N Baimpas in the Oxford University Department of Engineering Science. MM and TJM both acknowledge the support of Oxford Martin School and MM acknowledges the support of Linacre College at Oxford University, through a Junior Research Fellowship. The Manchester University X-Ray Imaging Facility (particularly Dr S.A. McDonald and Professor P.M. Mummery) is thanked for the loan of the loading rig for the I12 experiment. The WE43 Mg alloy was supplied by Magnesium Elektron Ltd, Manchester.

References

[1] Beghini M, Bertini L, Fontanari V. Evaluation of the stress-strain curve of metallic materials by spherical indentation. Int J Solids Struct. 2006;43:2441-59.

[2] Giannakopoulos AE, Larsson PL, Vestergaard R. Analysis of Vickers indentation. Int J Solids Struct. 1994;31:2679-708.

[3] Karthik V, Visweswaran P, Bhushan A, Pawaskar DN, Kasiviswanathan KV, Jayakumar T, et al. Finite element analysis of spherical indentation to study pile-up/sink-in phenomena in steels and experimental validation. Int J Mech Sci. 2012;54:7-83.

[4] Mesarovic SD, Fleck NA. Spherical indentation of elastic-plastic solids. Proc R Soc A-Math Phys Eng Sci. 1999;455:2707-28.

[5] Srikant G, Chollacoop N, Ramamurty U. Plastic strain distribution underneath a Vickers Indenter: Role of yield strength and work hardening exponent. Acta Mater. 2006;54:5171-8.

[6] Venkatesh TA, van Vleit KJ, Giannakopoulos AE, Suresh S. Determination of elasto-plastic properties by instrumented sharp indentation: guidelines for property extraction. Scr Mater. 2000;42:833-9.

[7] Busby JT, Hash MC, Was GS. The relationship between hardness and yield stress in irradiated austenitic and ferritic steels. J Nucl Mater. 2005;336:267-78.

[8] Deschamps A, Militzer M, Poole WJ. Precipitation Kinetics and Strengthening of a Fe-0.8wt%Cu Alloy. ISIJ Int. 2001;41:196-205.

[9] Kavanagh K, Clough RW. Finite element applications in the characterization of elastic solids. Int J Solids Struct. 1971;7:11-23.

[10] Fu J, Pierron F, Ruiz PD. Elastic stiffness characterization using three-dimensional full-field deformation obtained with optical coherence tomography and digital volume correlation. J Biomed Opt. 2013;18:1:16.
[11] Hild F, Roux S. Digital image correlation: From displacement measurement to identification of elastic properties - a review. Strain. 2006;42:69-80.
[12] Bay BK, Smith TS, Fyhire DP, Saad M. Digital volume correlation: three-dimensional strain mapping using X-ray tomography. Exp Mech. 1999;39:217-26.
[13] Cai B, Karagadde S, Yuan L, Marrow TJ, Connolley T, Lee PD. In situ synchrotron tomographic quantification of granular and intra-granular deformation during semi-solid compression of equiaxed dendritic Al-Cu alloys. Acta Mater. 2014;76:371-80.
[14] Mostafavi M, McDonald SA, Çetinel H, Mummery PM, Marrow TJ. Flexural strength and defect behaviour of polygranular graphite under different states of stress. Carbon. 2013;59:325-36.
[15] Mostafavi M, McDonald SA, Mummery PM, Marrow TJ. Observation and quantification of three-dimensional crack propagation in poly-granular graphite. Eng Fract Mech. 2013;110:410-20.
[16] Puncreobutr C, Lee PD, Hamilton RW, Cai B, Connolley T. Synchrotron Tomographic Characterization of Damage Evolution During Aluminum Alloy Solidification. Metall Trans A, Phys Metall Mater Sci. 2013;44:5389-95.
[17] Roux S, Hild F, Viot P, Bernard D. Three-dimensional image correlation from X-ray computed tomography of solid foam. Compos Pt A-Appl Sci Manuf. 2008;39:1253-65.
[18] Réthoré J, Limodin N, Buffière JY, Hild F, Ludwig W, Roux S. Digital volume correlation analyses of synchrotron tomographic images. J Strain Anal Eng Des. 2011;46:683-95.
[19] Mostafavi M, Baimpas N, Tarleton E, Atwood RC, McDonald SA, Korsunsky AM, et al. Thre-dimensional crack observation, quantification and simulation in a quasi-brittle material. Acta Mater. 2013;61:6276-89.
[20] Vertyagina Y, Mostafavi M, Reinhard C, Atwood RC, Marrow TJ. In situ quantitative three-dimensional characterisation of sub-indentation cracking in polycrystalline alumina. J Eur Ceram Soc. 2014;34:3127-32.
[21] Marrow TJ, Mostafavi M, Hashimoto T, Thompson GE. A quantitative three-dimensional in situ study of short fatigue crack in a magnesium alloy. Int J Fatigue. 2014.
[22] Truong V-T, Lai PK, Moore BT, Muscat RF, Russo MS. Corrosion protection of magnesium by electroactive polypyrroler/paint coatings. Synth Met. 2000;110:7-15.
[23] Staiger MP, Pietak AM, Hudamai J, Dias G. Magnesium and its alloys as orthopaedic biomaterials: A review. Biomaterials. 2006;27:1728-34.
[24] Kulekci MK. Magnesium and its alloys applications in automotive industry. Int J Adv Manuf Technol. 2008;39:851-65.
[25] Elecktron WE43. Magnesium Elektron Datasheet: 467. Manchester.
[26] McDanels DL. Analysis of stress-strain, fracture, and ductility behavior of aluminum matrix composites containing discontinuous silicon carbide reinforcement. Metall Trans A, Phys Metall Mater Sci. 1985;16:1105-6.
[27] http://physics.nist.gov/PhysRefData/Xcom/html/xcom1.html.

[28] Cloetens P, Pateyron-Salomé, Buffiere JY, Peix G, Baruchel J, Peyrin F, et al. Observation of microstructure and damage in materials by phase sensitive radiography. J Appl Phys. 1997;81:5878-87.
[29] Marrow TJ, Buffiere JY, Withers PJ, Johnson G, Engelberg DL. High resolution X-ray tomography of short fatigue crack nucleation in austempered ductile cast iron. Int J Fatigue. 2004;26:717-25.
[30] Titarenko V, Titarenko S, Withers PJ, De Carlo F, Xiao X. Improved tomographic reconstructions using adaptive time-dependent intensity normalization. J Synchrot Radiat. 2010;17:689-99.
[31] Munch B, Trtik P, Marone F, Stampanoni M. Stripe and ring artifact removal with combined wavelet—Fourier filtering. The International Online Journal of Optics. 2009;17:8567-91.
[32] DaVis. User's Manual. Gottingen: LaVision GmbH,; 2012.
[33] DE Man B, Nuyts J, Dupont P, Marchal G, Suetens P. Metal streak artifacts in X-ray computed tomography: A simulation study. IEEE Nuclear Science Symposium and Medical Imaging Conference Toronto, Canada: IEEE; 1998. p. 1860-5.
[34] Calcagnotto M, Ponge D, Rabbe D. Orientation gradients and geometrically necessary dislocations in ultrafine grained dual-phase steels studied by 2D and 3D EBSD. Mater Sci Eng, A. 2010;527:2738-46.
[35] Schwartz AJ, Kumar M, Adams BL, Field D. Electron backscatter diffraction in materials science: Springer; 2009.
[36] Sun Y, Bell T, Zheng S. Finite element analysis of the critical ratio of coating thickness to indentation depth for coating property measurement by nanoindentation. Thin Solid Films. 1995;258:198-204.
[37] ABAQUS. User's Manual: Dassault Systèmes Simulia Corp., Providence, Rhode Island, Version 6.10; 2010.
[38] Wilson CD. A critical reexamination of classical metal plasticity. J App Mech. 2001;69:63-8.
[39] Mostafavi M, Vertyagina Y, Reinhard C, Bradley R, Jiang XG, Galano M, et al. 3D studies of indentation by combined X-ray tomography and digital volume correlation. Key Eng Mater. 2014;592-593:14-21.
[40] Seo YH, Kang CG. Effects of hot extrusion through a curved die on the mechanical properties of SiCp/Al composites fabricated by melt-stirring. Compos Sci Technol. 1999;59:643-54.
[41] Kalidini SR, Pathak S. Determination of the effective zero-point and the extraction of spherical nanoindentation stress-strain curves. Acta Mater. 2008;56:3523-32.
[42] Donohue BR, Ambrus A, Kalidini SR. Critical evaluation of the indentation data analyses methods for the extraction of isotropic uniaxial mechanical propoerties using finite element models. Acta Mater. 2012;60.
[43] Pharr GM, Oliver WC. On the generality of the relationship among contact stiffness, contact area and elastic modulus during indentation. J Mater Res. 1992;7:613-7.
[44] Shoemaker K. Animating rotation with quaternion curves. In: Barsky BA, editor. Proceedings of SIGGRAPH '85. San Fransisco, CA, USA1985.

Figures

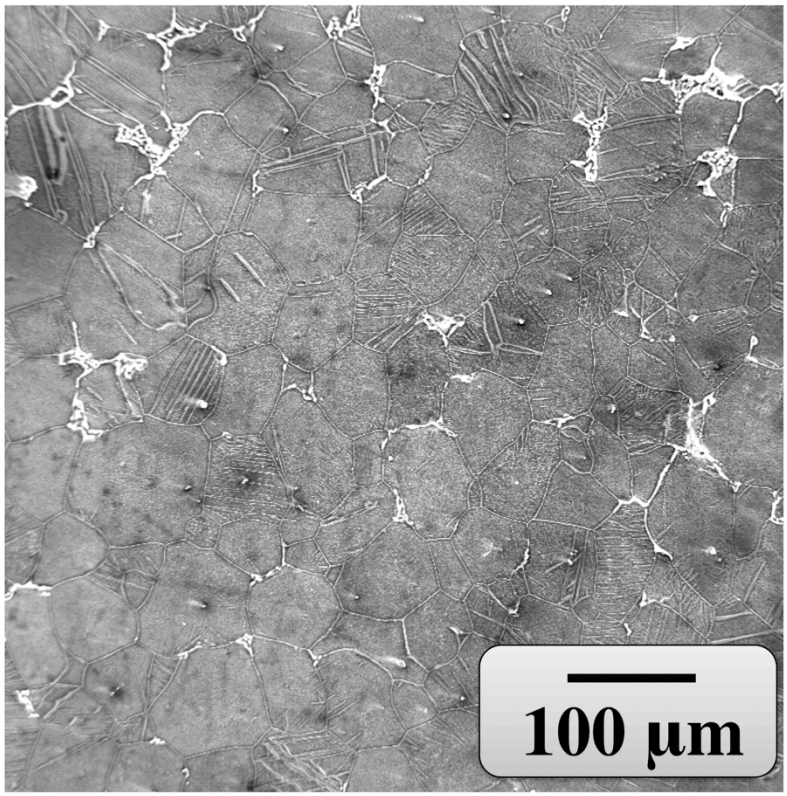

(a)

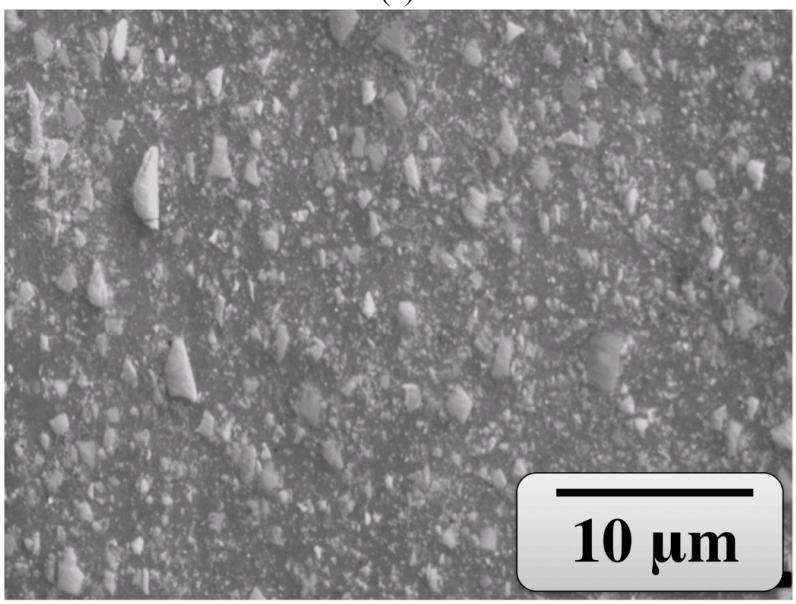

(b)

Figure 1 – Microstructures: (a) Mg alloy (Backscatter electron image) (b) Al-SiC (Secondary electron image)

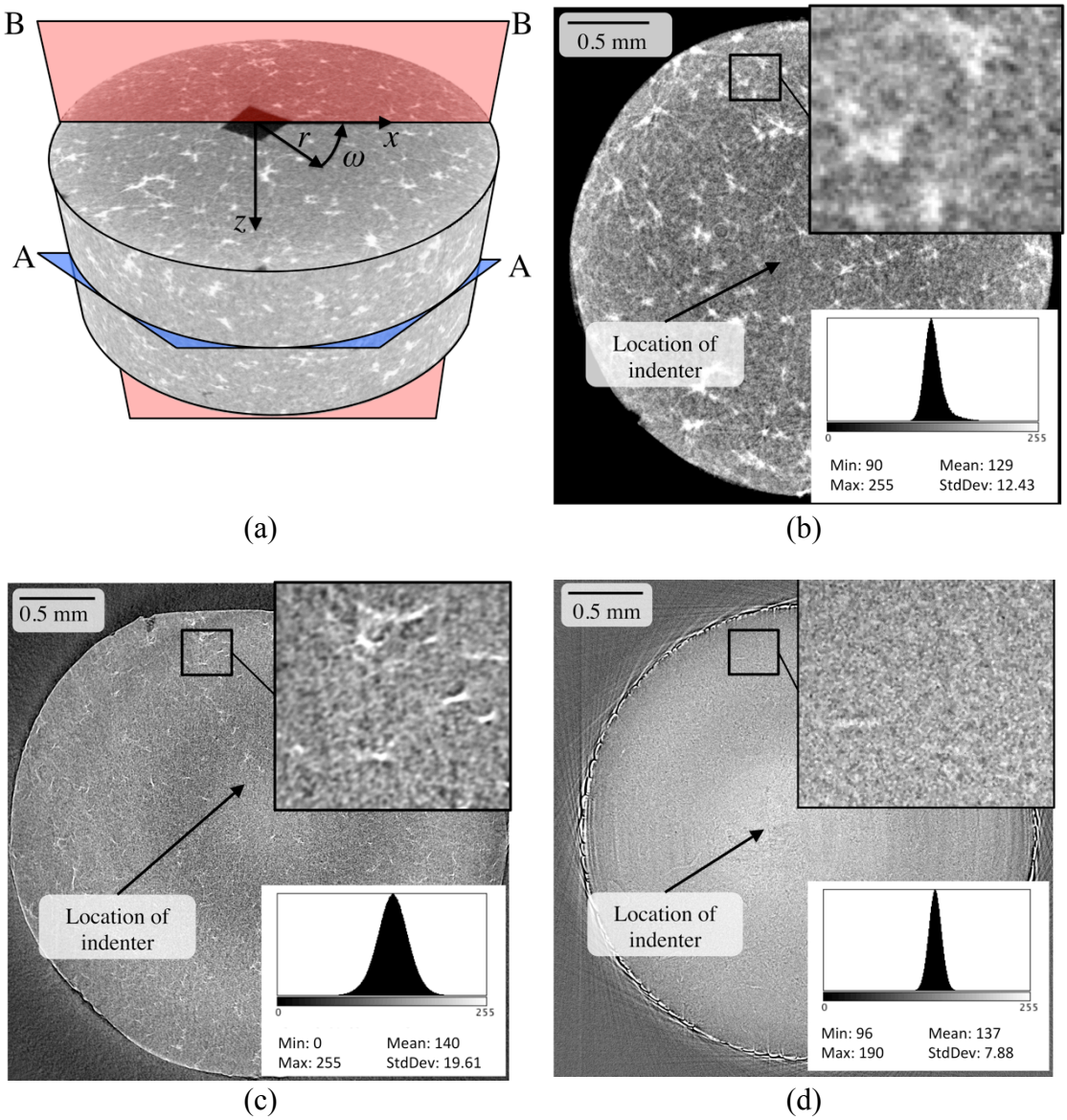

Figure 2 – (a) Definition of three-dimensional coordinates and cutting planes, on a reconstruction of the Mg alloy (laboratory tomography) and examples of virtual slices within the material on the horizontal AA plane for (b) Mg laboratory (c) Mg synchrotron (d) Al-SiC synchrotron. Higher magnification images to illustrate the resolution of the tomographs and histograms of image intensity are inset.

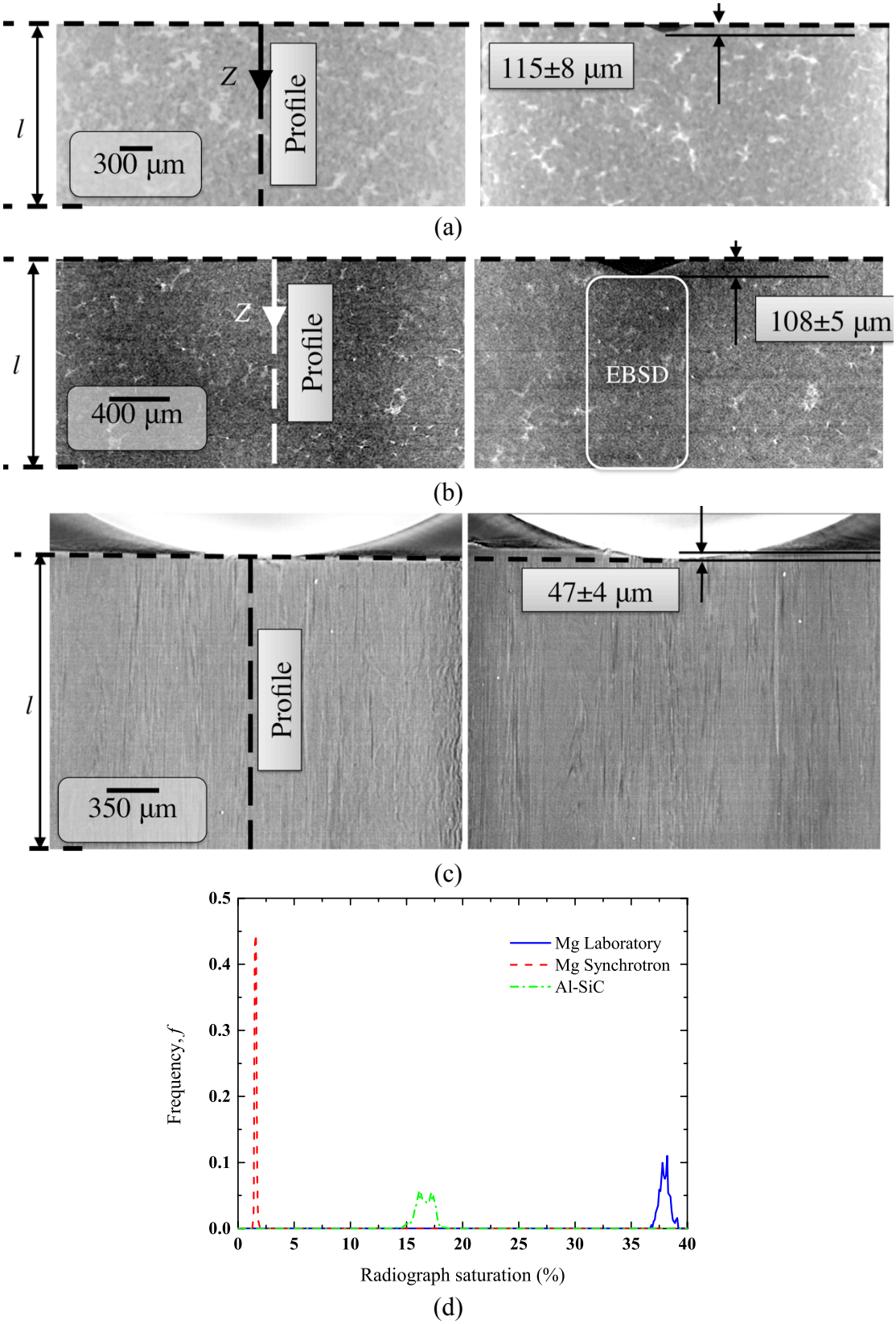

Figure 3 – Examples of a virtual slice in the BB plane before (left hand side) and after (right hand side) loading for (a) Mg alloy laboratory (b) Mg alloy synchrotron (c) Al-SiC synchrotron (d) normalised grey-scale distribution along the profiles shown in a, b and c (d) frequency distributions of the detector saturation along the same profiles in the X-ray radiographs.

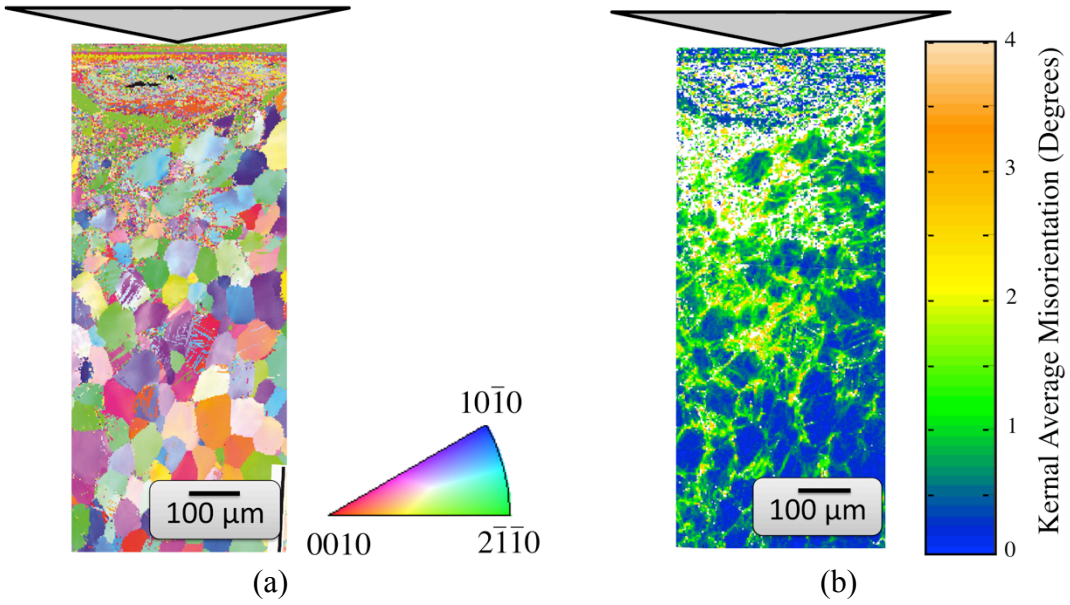

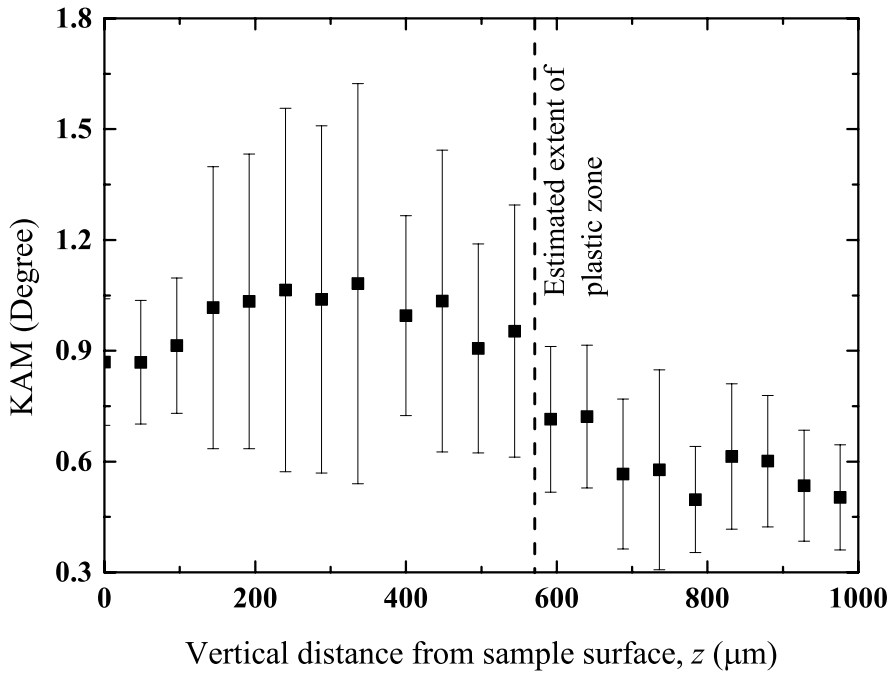

(c)

Figure 4: (a) EBSD map (black regions have not been indexed) and (b) Kernel average disorientation (white areas could not be analysed), measured on the BB plane parallel to the indentation direction passing through the deepest indentation point (see Figure 2) (c) Averaged KAM along a profile passing through the deepest point of the indentation

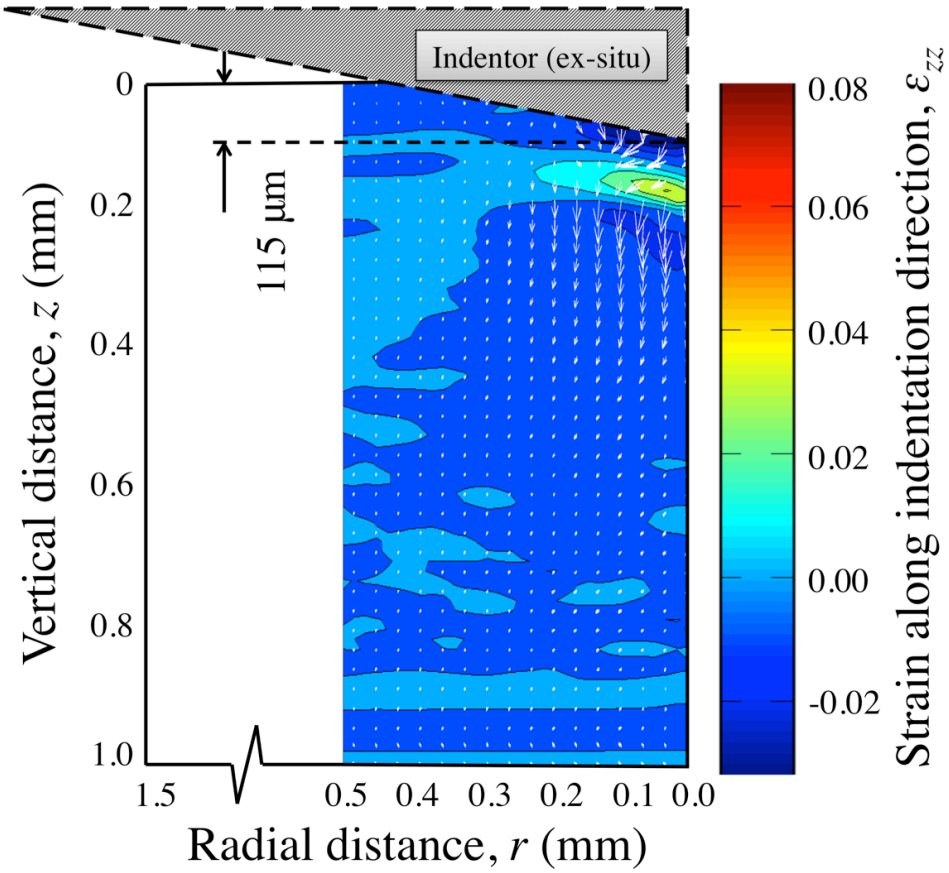
Indentor (ex-situ)
115 µm
Vertical distance, z (mm)
0
0.2
0.4
0.6
0.8
1.0
1.5
0.5
0.4
0.3
0.2
0.1
0.0
Radial distance, r (mm)
0.08
0.06
0.04
0.02
0.00
-0.02
Strain along indentation direction, ε_{zz}

(a)

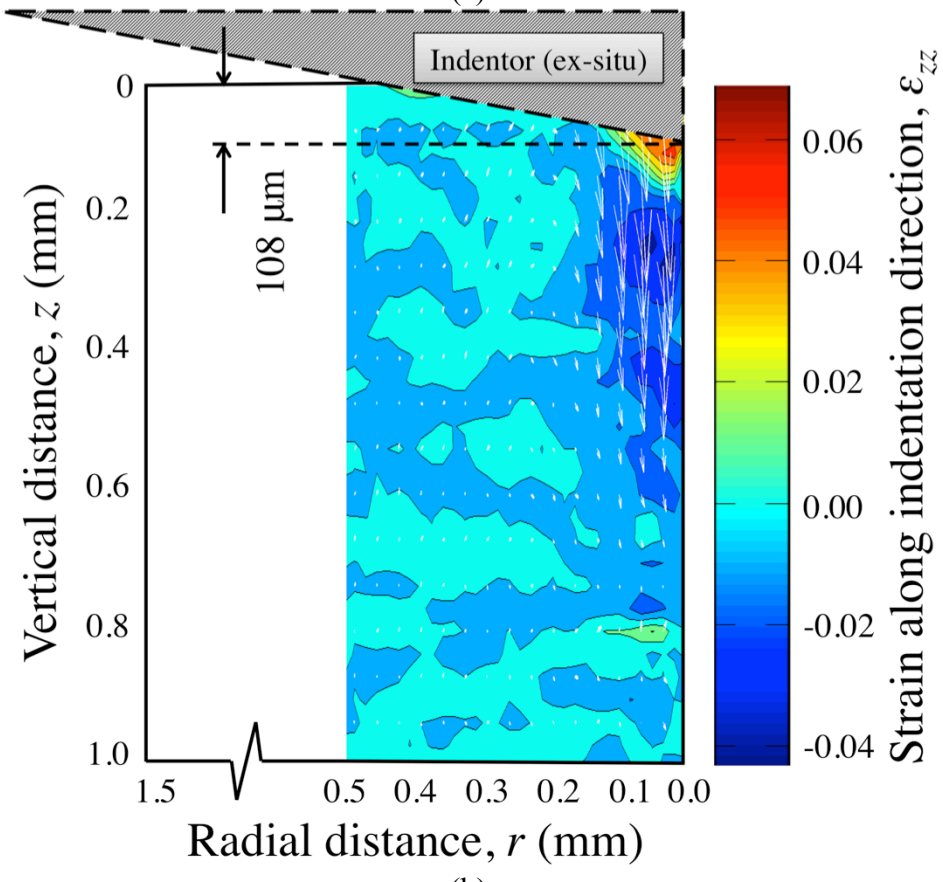
Indentor (ex-situ)
108 µm
Vertical distance, z (mm)
0
0.2
0.4
0.6
0.8
1.0
1.5
0.5
0.4
0.3
0.2
0.1
0.0
Radial distance, r (mm)
0.06
0.04
0.02
0.00
-0.02
-0.04
Strain along indentation direction, ε_{zz}

(b)

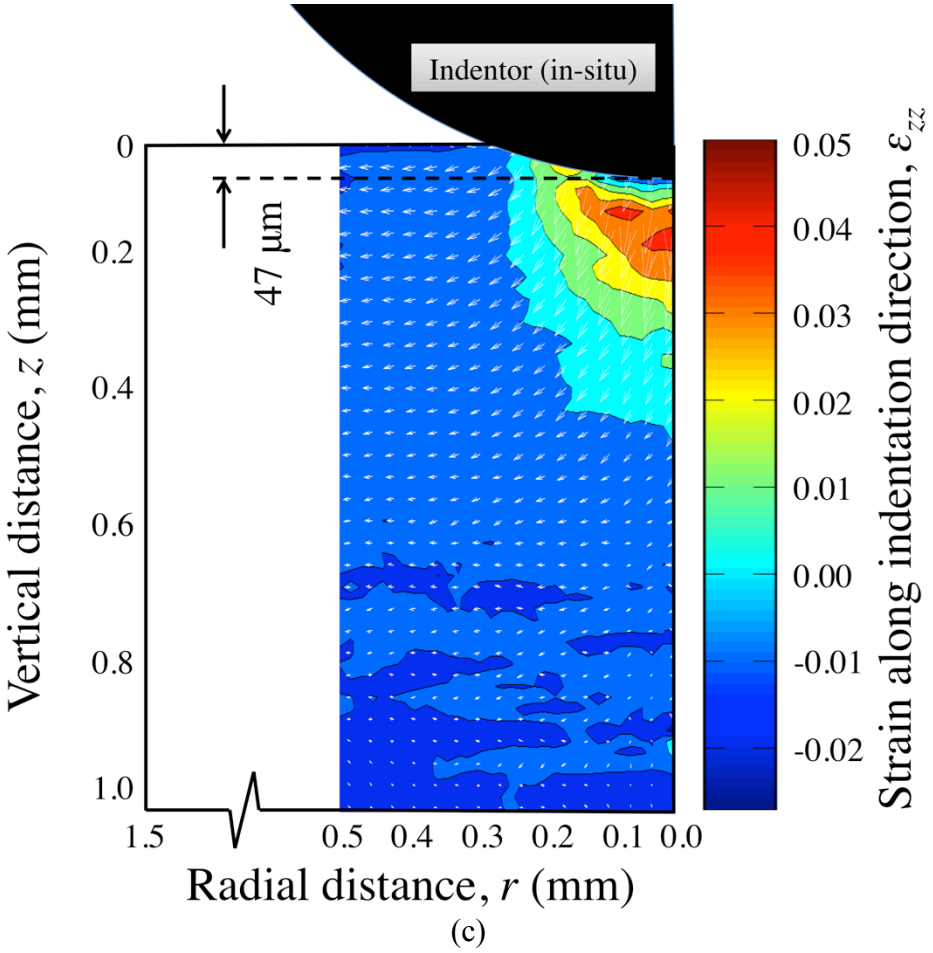

Figure 5: Visualisation of radially averaged displacement vectors and compressive strain distribution below the indenter in the BB plane at the centre of the indented region. The contours of compressive strain εzz and displacement vectors are shown for a) Mg laboratory test b) Mg synchrotron test and c) Al-SiC (Every fifth vector is shown, magnified 100 times for clarity)

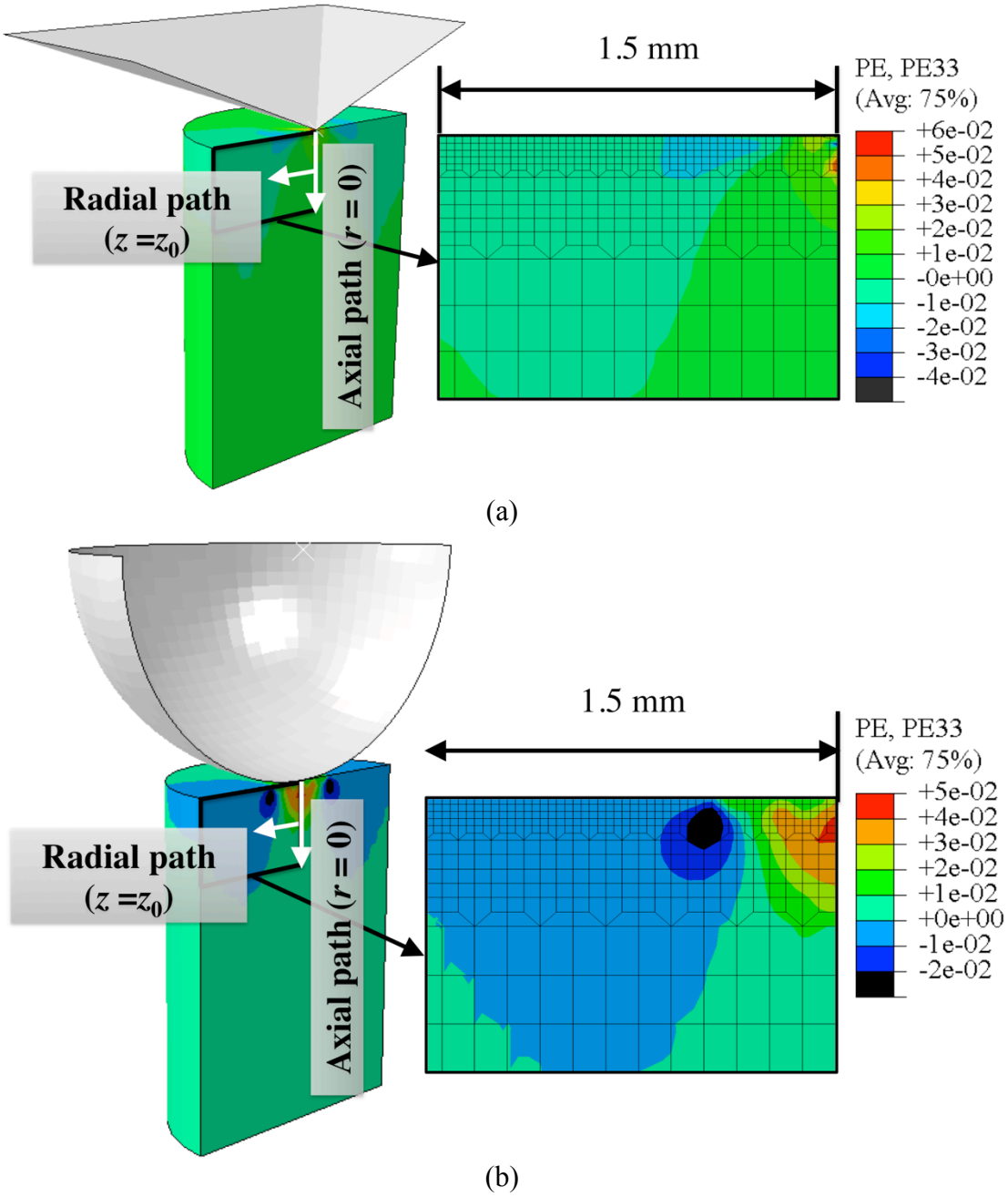

Figure 6: Overview of finite element model showing compressive strain in the BB section; (a) Vickers indentation on Mg after unloading (b) Hertzian indentation on Al-SiC at the peak load

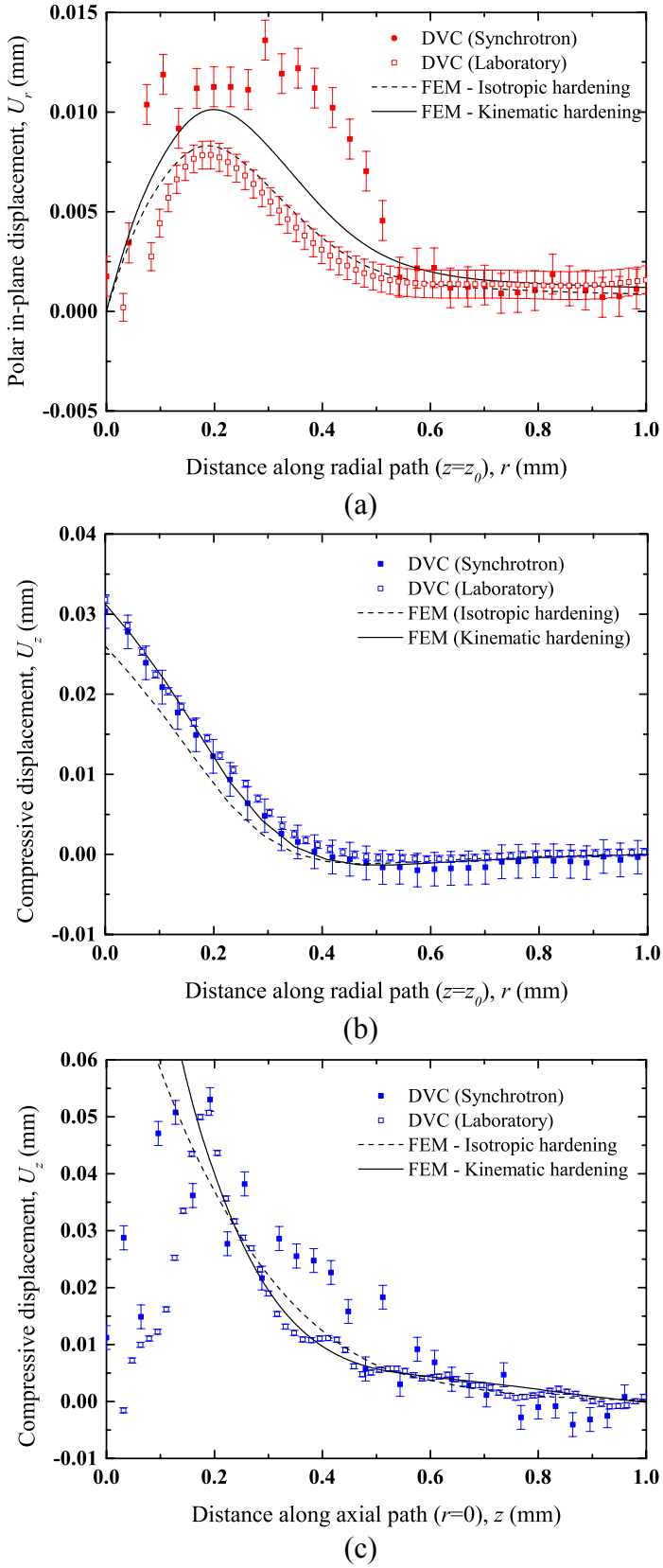

Figure 7: Displacements in Mg, measured experimentally by DVC of laboratory or synchrotron tomographs and calculated by finite element model (FEM) (for path definition see Figure 6); (a) radial displacement parallel to the radial path z = 256 µm below the surface (b) compressive displacement perpendicular to the same radial path (c) compressive displacement parallel to the axial path.

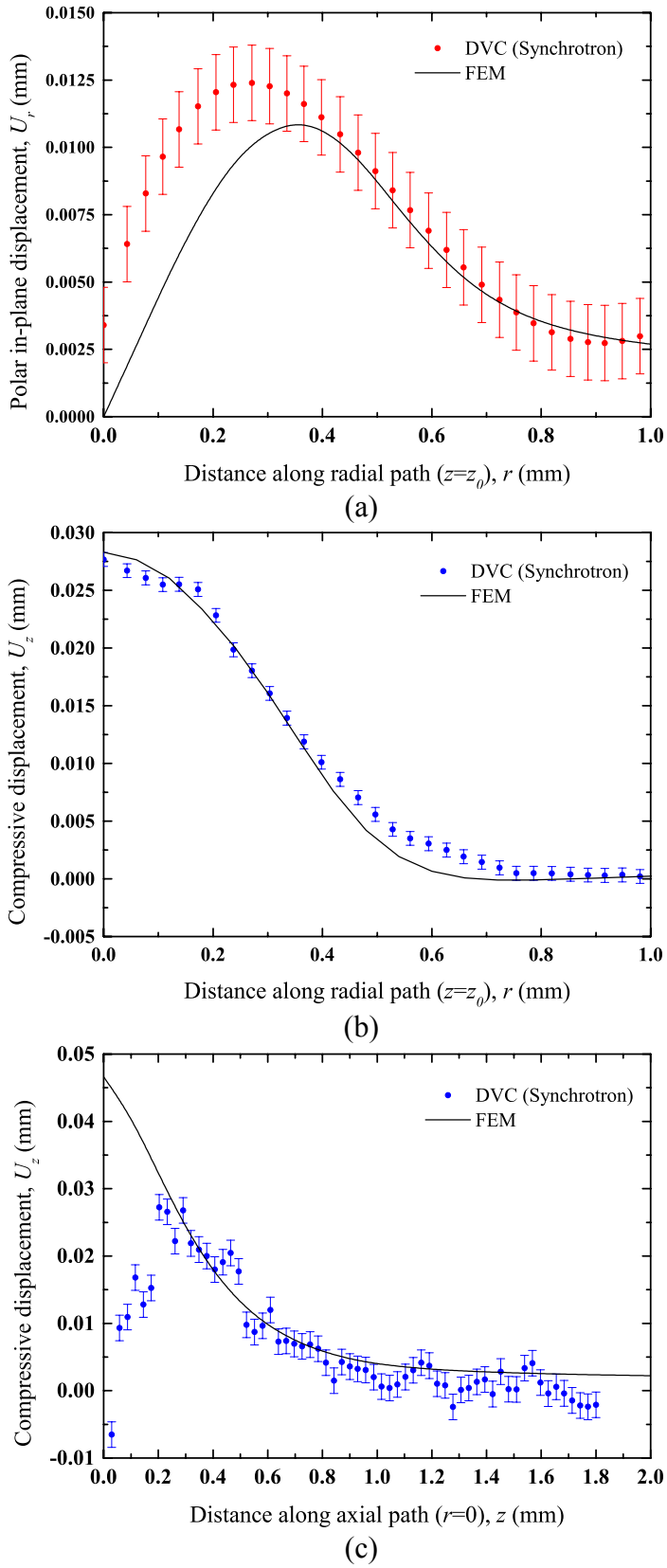

Figure 8: Displacements in Al-SiC, measured experimentally by DVC of laboratory or synchrotron tomographs and calculated by finite element model (FEM) (for path definition see Figure 6); (a) radial displacement parallel to the radial path z = 232 µm below the surface (b) compressive displacement perpendicular to the same radial path (c) compressive displacement parallel to the axial path.

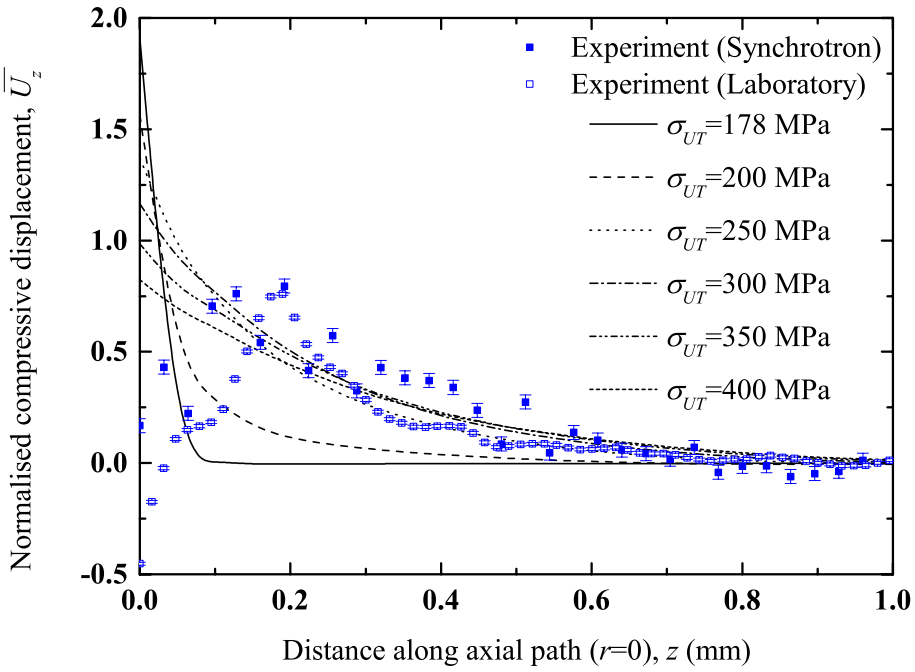
Normalised compressive displacement, $\overline{U}_z$
Distance along axial path (r=0), z (mm)
Experiment (Synchrotron)
Experiment (Laboratory)
σ_{UT}=178 MPa
σ_{UT}=200 MPa
σ_{UT}=250 MPa
σ_{UT}=300 MPa
σ_{UT}=350 MPa
σ_{UT}=400 MPa

(a)

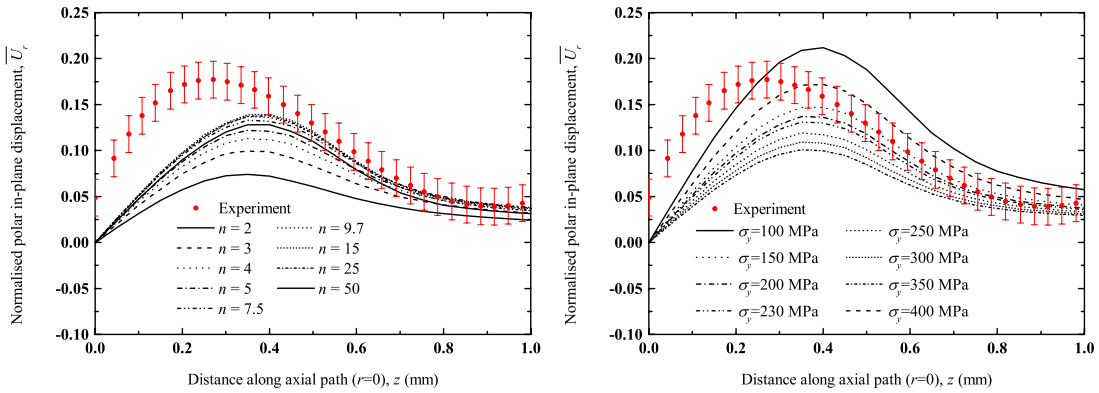
Normalised polar in-plane displacement, $\overline{U}_r$
Distance along axial path (r=0), z (mm)
Experiment
n = 2
n = 3
n = 4
n = 5
n = 7.5
n = 9.7
n = 15
n = 25
n = 50
Experiment
σ_y=100 MPa
σ_y=150 MPa
σ_y=200 MPa
σ_y=230 MPa
σ_y=250 MPa
σ_y=300 MPa
σ_y=350 MPa
σ_y=400 MPa

(b)

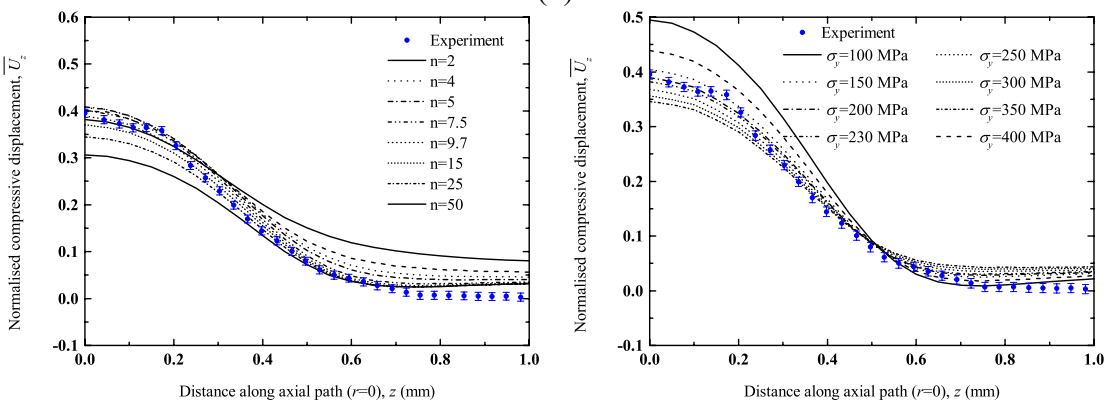
Normalised compressive displacement, $\overline{U}_z$
Distance along axial path (r=0), z (mm)
Experiment
n=2
n=4
n=5
n=7.5
n=9.7
n=15
n=25
n=50
Experiment
σ_y=100 MPa
σ_y=150 MPa
σ_y=200 MPa
σ_y=230 MPa
σ_y=250 MPa
σ_y=300 MPa
σ_y=350 MPa
σ_y=400 MPa

(c)

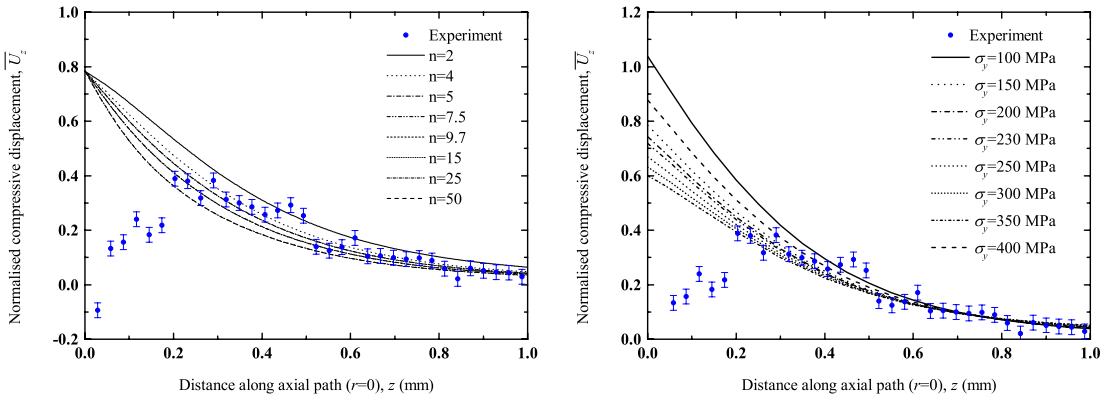

(d)

Figure 9: Sensitivity of compressive displacement to material properties (a) Normalised compressive displacement along the axial path for Mg alloy with kinematic hardening, constant yield stress (178 MPa), varying maximum tensile stress σ_{UT} (b) Normalised radial displacement along the radial path at z = 232 µm below the surface of Al-SiC with Ramberg-Osgood material model, different hardening exponent and yield stress (c) Normalised compressive displacement perpendicular to the radial path at z = 232 µm below the surface of Al-SiC with Ramberg-Osgood material model, different hardening exponent and yield stress (d) Normalised compressive displacement along the axial path for Al-SiC with Ramberg-Osgood material model, different hardening exponent and yield stress.

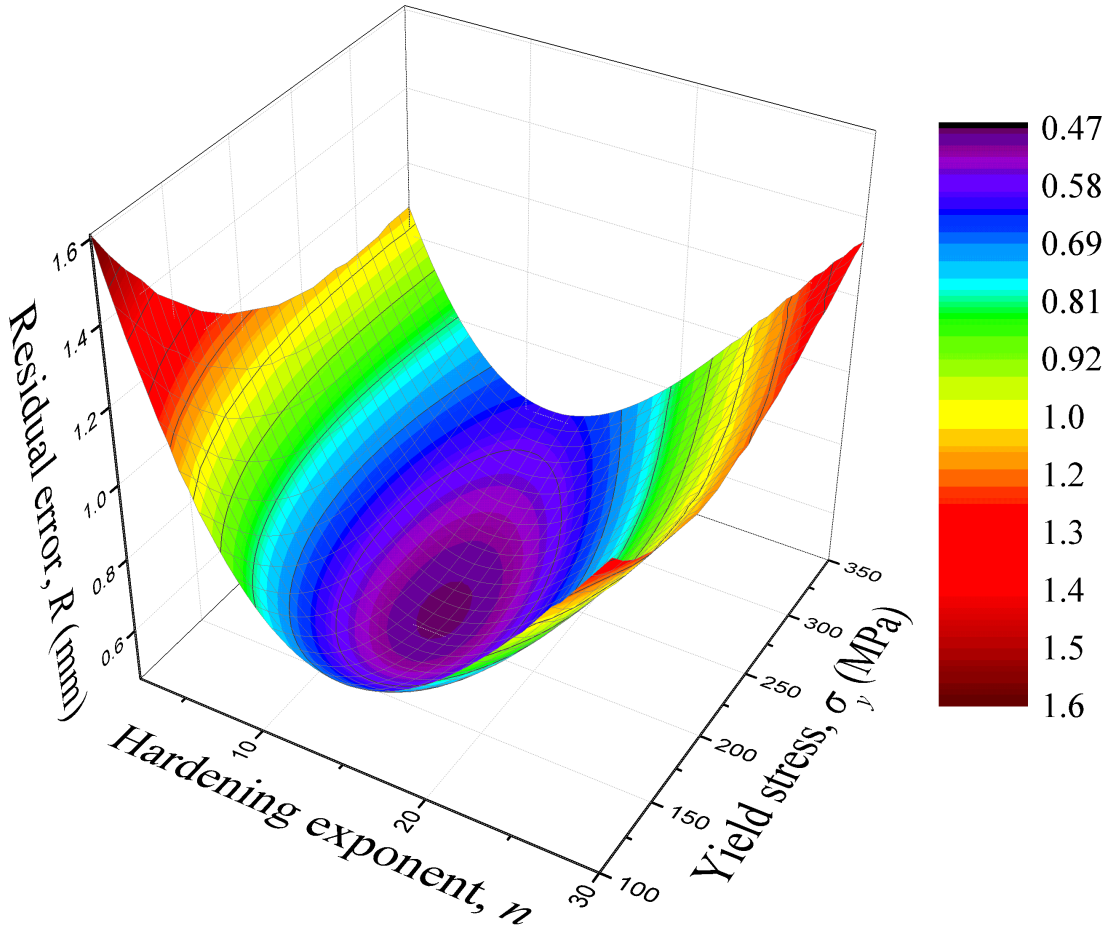

Figure 10: Contour representation of the residual error as a function of hardening exponent and yield stress; the residual error is obtained via comparison of the displacements along the axial path beneath the indentation for the FE simulation and experimental observation in the Al-SiC composite.

Appendix - Rigid Body Translation and Rotation Correction

The initial registering of images for DVC does not correct for sub-voxel size rigid body translations between the tomography datasets. For in situ mechanical experiments, there can be small three-dimensional rigid body rotations and displacements, caused by the tilting of the sample or flexure of the loading rig between tomography scans. Similarly, small displacements occur in ex situ experiments in which the sample is removed and replaced. If not properly accounted for, or corrected, these can impede the analysis of the deformation field.

An example from the Al-SiC composite experiment (Figure A1a), shows the relative in-plane displacement vectors overlaid on a contour map of the vertical compressive displacements for the horizontal (*AA)* plane that is approximately 200 μm below the indented surface. The coordinate system is defined by experiment, with the vertical axis parallel to the tomography rotation axis, which is also the nominal axis of the indentation. Vertical displacements have been corrected to one voxel precision by registration of horizontal image slices remove from the indentation. The relative rotation angle about the vertical axis, which is apparent in the displacement vectors in the figure, is approximately 3°. There also is a smaller (~0.5°) rotation about an orthogonal axis within the *xy* plane. It is preferable to consider the displacements (and components of strain) with respect to the reference frame of the sample, which is clearly slightly rotated relative to the measurement axis, otherwise the sample rotation effect can dominate the displacement field. This could be corrected by rotating one of the tomography datasets prior to DVC, using the precise rotation angles obtained by an initial DVC analysis with a large interrogation subset size. However, this is cumbersome for large datasets, involves interpolation of the images and also requires a further stage of image correlation to obtain the final result. Hence a computationally efficient method, based on [44], has been developed; this calculates the Euler rotation angles of the displacement field and uses these for its correction. In effect, the DVC measured displacement field (a very much smaller matrix) can then be rotated such that basement of the sample remote from the indentation presents only a rigid body movement (predominantly vertical); this is then readily corrected for.

The positions with respect to a reference Cartesian coordinates of the centres of the interrogation subsets, at which the displacement vectors are calculated, can be represented as $\left[X_i^o\right]=\left[x_i^o,y_i^o,z_i^o\right]$. After the deformation, their positions are denoted by $\left[X_i^1\right]=\left[x_i^1,y_i^1,z_i^1\right]$. The relative displacement vector for each point $\left[U_i\right]=\left[u_i^x,u_i^y,u_i^z\right]$ is defined as:

$$\left[U_i\right]=\left[X_i^1\right]-\left[X_i^o\right] \qquad 1$$

The first step in performing the correction for rigid body movements is to calculate the rigid body translation $\left[\bar{U}\right]=\left[\bar{u}^x,\bar{u}^y,\bar{u}^z\right]$:

$$\bar{u}^x = \frac{\sum_{i=1}^{n} u_i^x}{n}, \bar{u}^y = \frac{\sum_{i=1}^{n} u_i^y}{n}, \bar{u}^z = \frac{\sum_{i=1}^{n} u_i^z}{n} \quad 2$$

where n is the number of measured vectors. The centre of rigid body rotation ($\left[\bar{X}\right] = \left[\bar{x}, \bar{y}, \bar{z}\right]$) is assumed to be a point with zero rigid body translation, i.e. approximately at the point with the smallest value of $(\bar{u}^x - \bar{u}_i^x)^2 + (\bar{u}^y - \bar{u}_i^y)^2 + (\bar{u}^z - \bar{u}_i^z)^2$.

The reference coordinates of the centre of the interrogation subsets with respect to the centre of rotation are calculated by:

$$\left[X_i^{o,CT}\right] = \left[X_i^o\right] - \left[\bar{X}\right] \quad 3$$

The position of each point after deformation, corrected for rigid body translation is calculated by:

$$\left[X_i^{1,CT}\right] = \left[X_i^{o,CT}\right] + \left[U_i\right] - \left[\bar{U}\right] \quad 4$$

where CT stands for corrected translation. Assuming that the displacements due to deformation are negligible compared with the displacements due to rigid body rotation[2], the final position of each point with respect to its reference position can be described as:

$$\left[X_i^{1,CT}\right]_{n\times 3} = \left[X_i^{o,CT}\right]_{n\times 3} \left[M\right]_{3\times 3} \quad 5$$

i.e.

[2] In the case where deformation is significant, only those displacements in a part of the sample remote from the deformation might be considered.

$$\begin{bmatrix} x_1^{1,CT} & y_1^{1,CT} & z_1^{1,CT} \\ x_2^{1,CT} & y_2^{1,CT} & z_2^{1,CT} \\ x_3^{1,CT} & y_3^{1,CT} & z_3^{1,CT} \\ & & \\ x_n^{1,CT} & y_n^{1,CT} & z_n^{1,CT} \end{bmatrix} = \begin{bmatrix} x_1^{o,CT} & y_1^{o,CT} & z_1^{o,CT} \\ x_2^{o,CT} & y_2^{o,CT} & z_2^{o,CT} \\ x_3^{o,CT} & y_3^{o,CT} & z_3^{o,CT} \\ & & \\ x_n^{o,CT} & y_n^{o,CT} & z_n^{o,CT} \end{bmatrix} \begin{bmatrix} m_{11} & m_{12} & m_{13} \\ m_{21} & m_{22} & m_{23} \\ m_{31} & m_{32} & m_{33} \end{bmatrix} \quad 6$$

where n is the number of the calculated vectors and $[M]$ is a transformation matrix. If the Euler rotation is considered to be the result of a sequence of *yaw* (rotation around z axis, ϕ) followed by *pitch* (rotation around y axis, θ) then by *roll* (rotation around x axis, ψ), the conversion matrix can be represented as:

$$\bar{M} = \begin{bmatrix} \cos\theta\cos\phi & \cos\theta\sin\phi & -\sin\theta \\ \sin\psi\sin\theta\cos\phi - \cos\psi\sin\phi & \sin\psi\sin\theta\sin\phi + \cos\psi\cos\theta & \cos\theta\sin\psi \\ \cos\psi\sin\theta\cos\phi + \sin\psi\sin\phi & \cos\psi\sin\theta\sin\phi - \sin\psi\cos\phi & \cos\theta\cos\psi \end{bmatrix} \quad 7$$

A provisional conversion matrix can be extracted from the experimentally obtained data:

$$[M] = \left[X^{o,CT}\right]^{+}\left[X^{1,CT}\right] \quad 8$$

where $\left[X^{o,CT}\right]^{+}$ denotes the Moore-Penrose pseudo-inverse of $\left[X^{o,CT}\right]$. To avoid numerical instability, the ranks of matrices $\left[X^{o,CT}\right]$, $\left[X^{1,CT}\right]$ were calculated at this stage to ensure that none of the three singular values of each matrix are zero. As an additional check, $[M][M]^{T}$ was calculated to verify it is an identity matrix. The final rotation angles are extracted from the provisional rotation matrix using Kevin Shoemaker's method [44]:

$$\begin{aligned} \phi &= \text{atan2}\left(m_{12}, m_{11}\right) \\ \theta &= \text{atan2}\left(-m_{13}, \sqrt{m_{11}^2 + m_{12}^2}\right) \\ \psi &= \text{atan2}\left(m_{23}, m_{33}\right) \end{aligned} \quad 9$$

where $\text{atan2}(m_i, m_j)$ returns the angle between the positive x-axis of a plane and the point given by the coordinates (m_i, m_j); this enables the atan function to retune the appropriate quadrant of the computed angle.

Using Eqs. 7 and 9, the displacement due to rigid body rotation only is calculated by:

$$\left[\bar{X}^{1,CT}\right] = \left[X^{1,CT}\right]\left[\bar{M}\right] \tag{10}$$

Finally, the position of the centre of the interrogation subsets after correction for both rigid body translation and rotation $\left[X^{1,CT,CR}\right]$ is calculated from:

$$\left[X^{1,CT,CR}\right] = \left[X^{1,CT}\right] - \left[\bar{X}^{1,CT}\right] \tag{11}$$

And the displacement vector due to pure deformation (corrected for both translation and rotation) is calculated by:

$$\left[U_i^{CT,CR}\right] = \left[X_i^{1,CT,CR}\right] - \left[X_i^{o,CT}\right] \tag{12}$$

An in-house MATLAB® code was developed to correct for the rigid body translation and rotation of experimental data. The rotation angles obtained for the three experiments reported in this paper are given in Table A1 (θ, φ and ψ are the rotation angles around x, y and z axes respectively – see Figre2a). Data in all the parts of the sample were used considering the local effect of indentation, which affects a small area compared to the rest of the specimen. The displacements in the AA plane, after correction, are shown in Figure A1b; these are calculated relative to the average displacement of the sample at a position far from the indentation (i.e. at z = 1 mm). The deformation due to the indentation is now well visualised, particularly because the rotation about the axis in the xy-plane of ~ 0.5° has been removed. A further benefit is an improved estimate of the measurement uncertainty. Ideally, this should be obtained by analysis of a rigid body movement of an undeformed sample, but this is not always possible. Analysis of a part of a sample that has negligible deformation can then provide an estimate. The removal of the small gradient of displacement in this undeformed region of the sample, caused by sample rotation, reduces the measured range, which is then dominated by the measurement noise. The effect is shown in Table A2; correction for the rotations reduces the errors from order of 1 voxel to 0.5 voxel for Mg laboratory, from 8 voxels to 2 voxels for Mg synchrotron and from 7 voxels to 2 voxels for the Al-SiC.

Table A1 – Rigid body rotation angles

	θ (°)	φ (°)	ψ (°)
Mg (laboratory)	0.03	-0.01	-0.02
Mg (synchrotron)	-1.23	-1.33	0.58
Al-SiC	-0.30	0.57	2.84

Table A2 – Estimated displacement uncertainty

		Ur		*Uz*	
		voxel	µm	voxel	µm
Mg (laboratory)	AC	1.9	7.6	0.1	0.5
	RC	0.4	1.7	0.1	0 4
	RA	0.2	0.7	0.1	0.4
Mg (synchrotron)	AC	5.5	6.2	11.7	13.2
	RC	1.7	1.9	3.2	3.6
	RA	0.9	1.0	1.9	2.1
Al-SiC	AC	6.7	6.0	7.2	6.5
	RC	2.2	2.0	2.1	1.9
	RA	1.6	1.4	0.7	0.6

AC – As-Calculated (without rotation correction)

RC – Rotation Corrected

RA – Radially Averaged

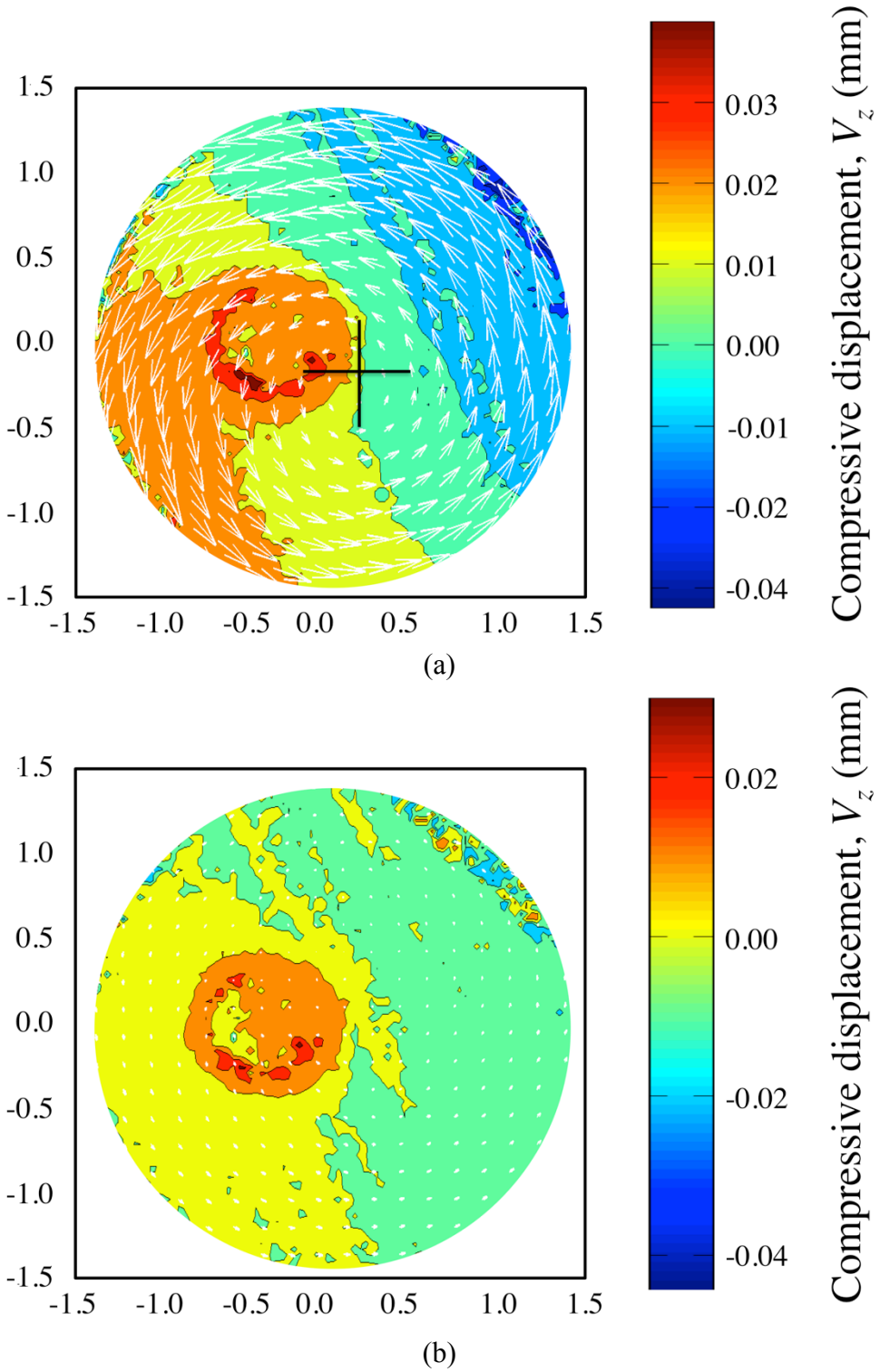

Figure A1: Vertical (U_z) displacement field in Al-SiC (values in mm) in *AA* plane 213 voxels (0.192 mm) below the indenter (a) Original – the approximate location of the axis of rotation around z axis is marked by + (b) Rigid body rotation corrected. The displacements are reported relative to the average displacement at a position far from the indentation (i.e. at z = 1 mm) to remove the small rigid body translations.